

– For internal NASA use only –

Lunar Meteoroid Ejecta Engineering Model

Anthony M. DeStefano
NASA MSFC EV44

March 31, 2022

Contents

1 Executive Summary	1
2 Lunar Regolith Properties	2
2.1 Porosity	2
2.2 Density	2
2.3 Strength	4
2.4 Particle Size Distribution	7
2.5 Scaling Law Parameters	11
3 Primary Flux Environment	11
3.1 Space-Time Dependence of Environment	11
3.1.1 Ephemeris Definition	12
3.2 Sporadic Meteoroid Complex	13
3.2.1 Angular Distribution	15
3.2.2 Density Distribution	19
3.2.3 Mass Distribution	21
3.3 Near-Earth Objects	21
3.3.1 Speed Distribution	22
3.3.2 Mass Distribution	22
3.4 Meteoroid Showers	23
4 Ejecta Flux from Impact Point	24
4.1 Ejecta Distribution	24
4.1.1 Speed Distribution	24
4.1.2 Zenith Distribution	24
4.1.3 Azimuth Distribution	26
4.2 Mass/Particle Size Distribution	26
4.2.1 NASA SP-8013	27

4.2.2	O'Keefe & Ahrens 1985	29
4.3	Orbital Mechanics	30
4.3.1	Crater on Surface to Observer at Surface	30
4.3.2	Crater on Surface to Observer at or above Surface	30
4.4	Selenographic Distance & Bearing	30
5	Scaling Laws	31
5.1	Crater Size – Strength & Gravity Regime	31
5.2	Minimum & Maximum Ejected Speed	31
5.3	Maximum Ejected Particle Mass	31
5.4	Mass Ejected from Crater	31
6	Secondary Environment at Asset	31
6.1	Latitude-Longitude Dependence	31
6.2	Speed Distribution	31
6.3	Angular Distribution	31
6.4	Ejecta Size Distribution	31
References		32

List of Figures

1	A comparison of the regolith bulk density for a certain depth (blue), the depth-averaged bulk density (orange), and the volume-averaged bulk density (green). See also, Figure 9.16 of the Lunar Sourcebook [Heiken <i>et al.</i> , 1991].	3
2	Relative error of using the density at a certain depth (blue) and using the depth-weighted average (orange) of the regolith bulk density.	5
3	The range of regolith shear strength as a function of depth below the lunar surface taken from Figure 9.26 of the Lunar Sourcebook. The average shear strength is also calculated (green). Points that are extrapolated beyond what is available are shown by the dashed lines. The volume-averaged shear strength (red) assumes a parabolic-shaped crater of depth z	6
4	Geotechnical particle size distribution: middle curve showing the average distribution; left-hand and right-hand curves showing ± 1 standard deviation [Carrier <i>III</i> , 2003]. Note, that the percent passing is normalized by mass and not particle number [see Carrier, 1973].	7
5	Plots of the mass-weighted and number-weighted CDFs and PDFs derived from Carrier <i>III</i> [2003]. Top left: the digitized data from Figure 1 of Carrier <i>III</i> [2003] is shown with the log-normal distribution fit. Top right: The mass-weighted PDF * dx is shown to dictate what particle size dominates the contribution of mass. Bottom left: The number-weighted CDF showing number of particles in 1 kg of regolith greater than a size x . Bottom right: The number-weighted PDF is shown in units of mm^{-1}	9

6	Fluxes at the meridional plane (as a function of impact speed and angle from the horizon) of the low density population (a) and (b), and the high density population (c) and (d) impacting the Moon at the equator (a) and (c), and the north/south pole (b) and (d).	14
7	Fluxes at the meridional plane as a function of approaching angle for the low density population (a) and (b), and the high density population (c) and (d) impacting the Moon at the south pole in a Mollweide (a) and (c), and all-sky (b) and (d) projection.	16
8	Fluxes at the meridional plane as a function of approaching angle for the low density population (a) and (b), and the high density population (c) and (d) impacting the Moon at -45° latitude in a Mollweide (a) and (c), and all-sky (b) and (d) projection.	17
9	Fluxes at the meridional plane as a function of approaching angle for the low density population (a) and (b), and the high density population (c) and (d) impacting the Moon at the equator in a Mollweide (a) and (c), and all-sky (b) and (d) projection.	18
10	Meteoroid density distribution according to the MEM3 User Guide. The apex and toroidal meteoroid sources constitute the low-density population, while the helion/antihelion source constitutes the high-density population. Each set of densities follows a log-normal distribution [c.f. Figure 11, <i>Moorhead et al.</i> , 2019].	19
11	Non-linear fit of the low density profile in Figure 10 with Eq. 3.2 in SciDAVis, giving the constants for $a \rightarrow A$, $s \rightarrow \sigma$, and $m \rightarrow \mu_\delta$	20
12	Non-linear fit of the high density profile in Figure 10 with Eq. 3.2 in SciDAVis, giving the constants for $a \rightarrow A$, $s \rightarrow \sigma$, and $m \rightarrow \mu_\delta$	20
13	The Grün interplanetary meteoroid flux as a function of limiting particle mass [<i>Moorhead et al.</i> , 2019, Figure 1], normalized to 1 for a limiting mass equal to or greater than $1\mu\text{g}$	21
14	Mass-limited speed distribution at the lunar surface.	22
15	Meteor shower flux (variable lines) and sporadic meteoroid flux (horizontal lines) over the course of 2021. Fluxes are quoted to four limiting particle kinetic energies; these kinetic energies correspond to particles with diameters of 0.04 cm, 0.1 cm, 0.3 cm, and 1 cm, assuming a density of 1 g cm^{-3} and a speed of 20 km s^{-1} , [see Figure 1, <i>Moorhead et al.</i> , 2020].	23
16	Average cumulative lunar ejecta flux-mass distribution for each of three ejecta velocity intervals [<i>Cour-Palais</i> , 1969].	28

List of Tables

1	Porosity for various depths.	2
2	The change of the shear strength of the lunar soil with depth.	5
3	Digitized data points from Figure 4, see <i>Carrier III</i> [2003].	8
4	Summary of constants used in the <i>Housen and Holsapple</i> [2011] ejecta model.	11

5	Cone angles of upstream and downstream of impact derived from Figure 18 of <i>Gault and Wedekind [1978]</i>	25
6	A compilation of indices of the various particle size distribution descriptions. Values that are in bold are the index that was originally used in the corresponding source.	27

Listings

1	An example email that is sent to JPL Horizons to compute an ephemeris file that is centered on the Moon at a location of 90° longitude, -65° latitude, and 0.6 km above the surface for 11 years.	12
2	Python script to convert JPL Horizons ephemeris file type to be read into the Meteoroid Engineering Model.	12

1 Executive Summary

2 Lunar Regolith Properties

2.1 Porosity

The lunar regolith porosity is related to the amount of free space between individual grains. The greater the porosity, the more void space is present. Table 3.4.2.3.4-1 of the DSNE gives values of the porosity as a function of depth down to 60 cm derived from Apollo core measurements (copied from Table 9.5 of the Lunar Sourcebook, *Heiken et al.* [1991]) and shown here in Table 1.

Table 1: Porosity for various depths.

Depth Range (cm)	Average Porosity, n (%)
0 – 15	52 ± 2
0 – 30	49 ± 2
30 – 60	44 ± 2
0 – 60	46 ± 2

2.2 Density

The bulk density (ρ) of the lunar regolith is defined as the mass of material in a given volume, which relates the particle density (ρ_p) and porosity (n) to the bulk density as (see Section 3.4.2.3.1 of the DSNE or Chapter 9 of the Lunar Sourcebook)

$$\rho = \rho_p(1 - n). \quad (2.1)$$

The DSNE suggests using $\rho_p = 3.1 \text{ g/cm}^3$ for the average particle density over the entire Moon. Otherwise, the typical highlands particle density is $\rho_p = 2.75 \pm 0.1 \text{ g/cm}^3$ whereas the typical mare particle density is $\rho_p = 3.35 \pm 0.1 \text{ g/cm}^3$.

The bulk density¹ as a function of depth, fit to Apollo data, is given by

$$\rho(z) = 1.92 \frac{z + 12.2}{z + 18}, \quad (2.2)$$

where z is the depth in cm and ρ is in units of g/cm^3 . At the surface ($z = 0$), the density is 1.30 g/cm^3 , and increases to 1.92 g/cm^3 for large depths. This expression is fairly reasonable down to 3 m (the limit reached by Apollo drill core samples). In order to get an up-to-depth average of the bulk density, take

$$\rho_{avg,depth}(z) = \frac{1}{z} \int_0^z dz' \rho(z'), \quad (2.3)$$

which gives (compare with the equation for d_m on page 494 of the Lunar Sourcebook)

$$\rho_{avg,depth}(z) = 1.92 \left[1 - \frac{5.8 \ln \left(\frac{z+18}{18} \right)}{z} \right]. \quad (2.4)$$

¹Follows the average particle density of 3.1 g/cm^3 for all depths with a porosity depth dependence following Table 1, see the *porosity of lunar soil* paragraph on page 492 in the Lunar Sourcebook.

For example, the average bulk density of the regolith with a depth range of 0 – 60 cm would be $\rho_{avg,depth}(60) = 1.65 \text{ g/cm}^3$.

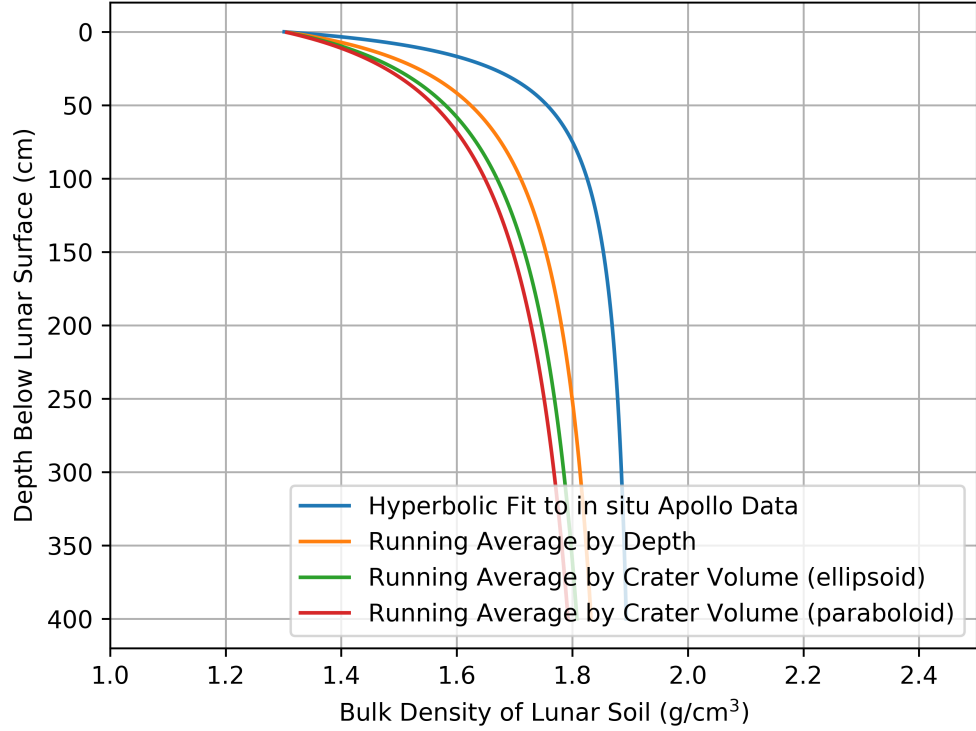


Figure 1: A comparison of the regolith bulk density for a certain depth (blue), the depth-averaged bulk density (orange), and the volume-averaged bulk density (green). See also, Figure 9.16 of the Lunar Sourcebook [[Heiken et al., 1991](#)].

For a higher-fidelity estimate of the average bulk density sampled by the crater, a volume-average can be used instead of a depth-average, given by

$$\rho_{avg,volume}(z) = \frac{\int dV \rho(z')}{\int dV}. \quad (2.5)$$

Expanding the integral in a cylindrical coordinate system and assuming an ellipsoidal crater shape, Equation (2.5) becomes

$$\rho_{avg,ellipsoid}(z) = \frac{\int_0^z \int_0^R \int_0^{2\pi} d\phi r dr dz' \rho(z')}{\int_0^z \int_0^R \int_0^{2\pi} d\phi r dr dz'} \quad (2.6)$$

$$= \frac{1.92}{4z^3} \left[z(6ab - 6b^2 - 3az + 3bz + 4z^2) + 6(a-b)(b^2 - z^2) \ln \left(\frac{b}{z+b} \right) \right], \quad (2.7)$$

for the volume-averaged density in g/cm³ with z in cm, where $a = 12.2$ and $b = 18$. Following the example from earlier, the average bulk density of the regolith with a depth range of 0 – 60 cm would be $\rho_{avg,ellipsoid}(60) = 1.60$ g/cm³, which is ~ 3% less than $\rho_{avg,depth}(60) = 1.65$ g/cm³.

On the other hand, if a paraboloid crater shape is assumed, Equation (2.5) becomes

$$\rho_{avg,paraboloid}(z) = \frac{\int_0^z \int_0^{R\sqrt{1-z'/z}} \int_0^{2\pi} d\phi r dr dz' \rho(z')}{\int_0^z \int_0^{R\sqrt{1-z'/z}} \int_0^{2\pi} d\phi r dr dz'} \quad (2.8)$$

$$= \frac{1.92}{z/2} \left[b - a + \frac{z}{2} - \frac{(a-b)(b+z) \ln\left(\frac{b}{z+b}\right)}{z} \right], \quad (2.9)$$

using the same values for a and b as before. Again, with the prior example, the average bulk density of the regolith with a depth range of 0 – 60 cm would be $\rho_{avg,paraboloid}(60) = 1.58$ g/cm³, which is ~ 4% less than $\rho_{avg,depth}(60) = 1.65$ g/cm³, see Figure 2. The expression given in Equation (2.9) is useful for computing the ejected mass from a crater², given a crater depth z .

The expressions for the regolith density at a certain depth z , weighted by depth, and weighted by crater volume (ellipsoid and paraboloid) are given by Equations (2.2), (2.4), and (2.7), (2.9), respectively, are compared in Figure 1. The crater volume is approximated as a half-ellipsoid with two of the dimensions scaled by the crater radius R and one dimension scaled by the crater depth z , sliced such that the half-ellipsoid is symmetric about the surface normal for Equation (2.7). On the other hand, a paraboloid-shaped crater is used for Equation (2.9). For a given crater, more of the volume is near the surface so that more weight is given by bulk densities that originate near the surface. In contrast, the depth-averaged bulk density takes the bulk density at each depth equally. This results in the volume-averaged bulk density to be slightly less than the depth-averaged bulk density, as shown in Figure 1. In addition, comparing an ellipsoidal crater vs. a parabolic crater, the parabolic crater (typically used in literature, see [Singer et al. \[2020\]](#)) exhibits the softest increase of the average bulk density as a function of depth.

2.3 Strength

The strength of the regolith can be measured in different ways, depending on the use. In the case of modeling impacts, the shear strength of loose regolith and tensile strength of solid rock can be used. The top 10 m or so consists of fine-grained material called regolith. From 10 m to about 2 km is the large scale ejecta that is course grained and ballistically transported (Fig 4.22 of the Lunar Sourcebook, [Heiken et al. \[1991\]](#)). All of the impacts studied in this model will create craters less than 2 km, so it is expected that the shear strength will be used for the loose regolith and large scale ejecta material.

²In an iterative fashion, since the crater radius depends on the regolith density.

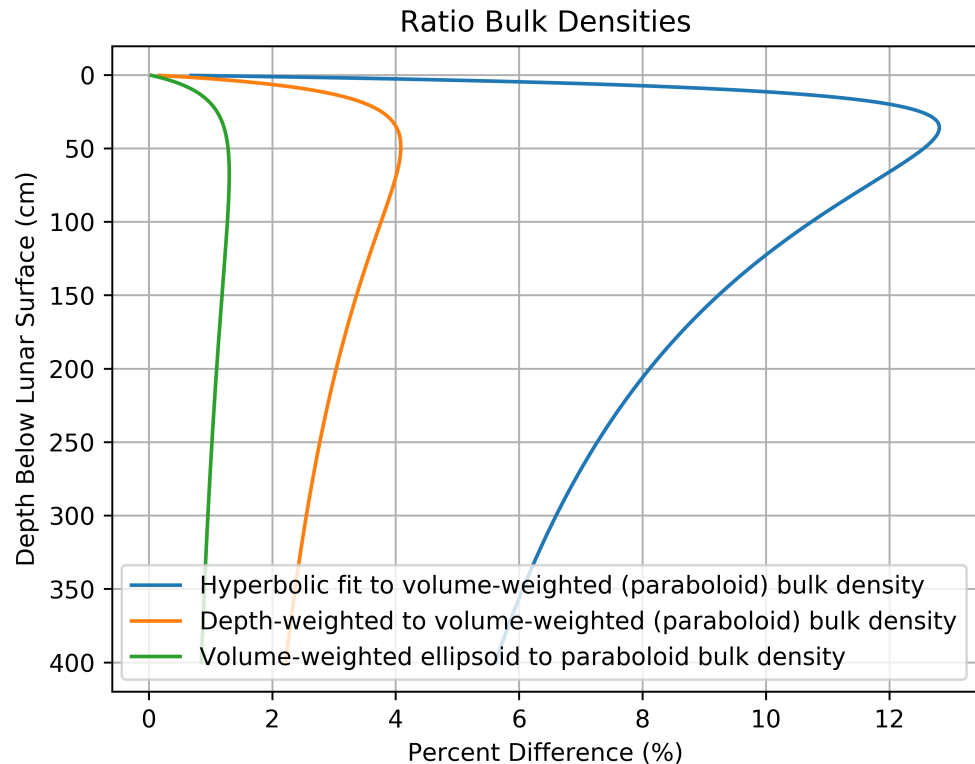


Figure 2: Relative error of using the density at a certain depth (blue) and using the depth-weighted average (orange) of the regolith bulk density.

The shear strength of the lunar soil increases with the depth. As an example, both Figure 9.26 of the Lunar Sourcebook, reproduced in Figure 3, and Table 12 of [Slyuta \[2014\]](#) depict this characteristic, shown in Table 2.

Table 2: The change of the shear strength of the lunar soil with depth.

Depth (cm)	Shear strength (kPa)
5	0.1 – 2.5
50	1 – 3.5
100	2 – 4
200	4 – 8

The average shear strength (green curve) in Figure 3 can be expressed by the

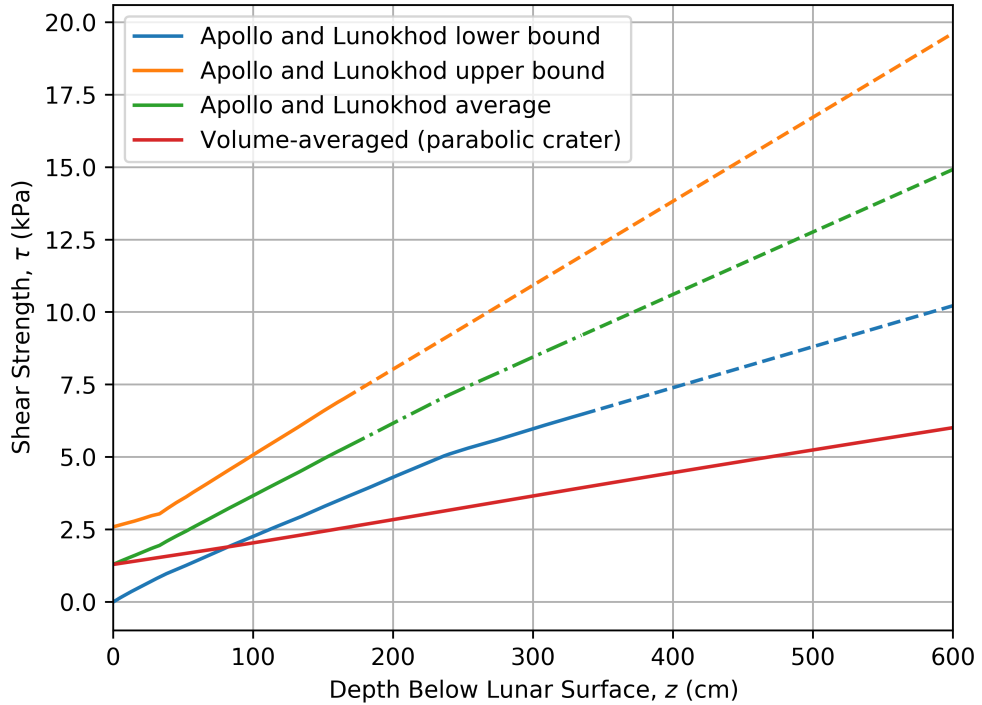


Figure 3: The range of regolith shear strength as a function of depth below the lunar surface taken from Figure 9.26 of the Lunar Sourcebook. The average shear strength is also calculated (green). Points that are extrapolated beyond what is available are shown by the dashed lines. The volume-averaged shear strength (red) assumes a parabolic-shaped crater of depth z .

piece-wise form

$$\tau(z) = \begin{cases} \frac{z}{45.55} + 1.288, & 0 \leq z < 50 \text{ cm} \\ \frac{z}{40.21} + 1.144, & 50 \text{ cm} \leq z < 250 \text{ cm} \\ \frac{z}{46.06} + 1.942, & z \geq 250 \text{ cm} \end{cases} . \quad (2.10)$$

Assuming the crater has a parabolic shape and that the effective shear strength is the volume-average (similar approach to Equation (2.5)), Equation (2.10) becomes (as shown by the red curve in Figure 3)

$$\tau(z) = \begin{cases} \frac{z}{136.65} + 1.288, & 0 \leq z < 50 \text{ cm} \\ \frac{z}{120.63} + 1.144 + \frac{7.163}{z} - \frac{118.33}{z^2}, & 50 \text{ cm} \leq z < 250 \text{ cm} \\ \frac{z}{138.18} + 1.942 - \frac{194.81}{z} + \frac{16902}{z^2}, & z \geq 250 \text{ cm} \end{cases} . \quad (2.11)$$

2.4 Particle Size Distribution

The cumulative distribution function (CDF) of the regolith particle sizes³ are fit to several Apollo samples, as shown in Figure 4. During an impact, the particle size distribution may become modified and are organized depending on the ejected speed (see Section 4.2). However, the unmodified regolith size distribution is given in this section for reference. The digitized data from Figure 4 is shown in Table 3.

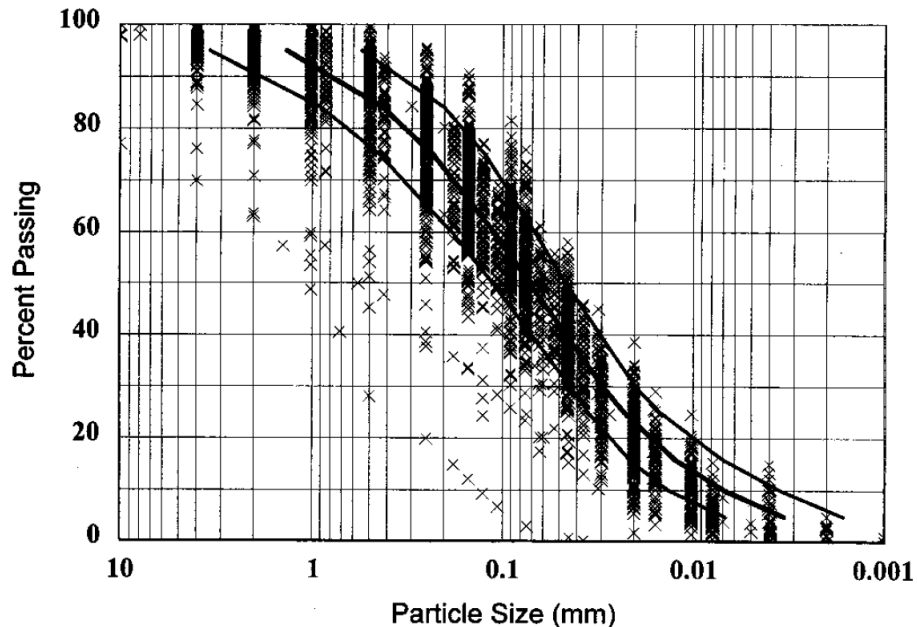


Figure 4: Geotechnical particle size distribution: middle curve showing the average distribution; left-hand and right-hand curves showing ± 1 standard deviation [Carrier III, 2003]. Note, that the percent passing is normalized by mass and not particle number [see Carrier, 1973].

In [Carrier III \[2003\]](#), they specifically call out that the mass-weighted CDF can be modeled by a log-normal distribution, so this assumption is made below. By definition, a log-normal distribution is given by

$$F_{\text{kg}}(>x) = 1 - F(<x)_{\text{kg}} = \frac{1}{2} \left[1 - \text{erf} \left(\frac{\ln x - \mu}{\sqrt{2}\sigma} \right) \right], \quad (2.12)$$

where x is the particle diameter size in units of mm, μ is the expected value of $\ln x$, and σ is the standard deviation of $\ln x$.

³In the context here, particle size is defined as the particle diameter of a spherical-shaped particle. Other sections may define size by the radius.

Table 3: Digitized data points from Figure 4, see *Carrier III [2003]*.

Particle Diameter (mm)	Cumulative Percent by Mass
0.003380248352585	5.17682028091534
0.003794441295246	6.09401642297017
0.00451292465605	7.2776812909626
0.0053674729594	8.4354410787182
0.006383732464611	9.71063723021409
0.007592176031253	11.2086170717467
0.009029116435596	12.9190185712213
0.010737989052827	14.65100763756
0.012769865152208	16.6247774527757
0.015185144104918	19.116648872728
0.018057261192048	21.6025237463292
0.02136872870221	24.2948870610798
0.025044648784976	27.0334149904509
0.029494364580794	29.8741284657866
0.033098954040892	32.8807708128992
0.037145453042138	35.6150479687852
0.042499223173782	38.2089250804786
0.048155933590968	41.1181012805662
0.054042887826956	43.8970091889745
0.060942690951498	46.6685810695819
0.068720899309714	49.7075873197331
0.077869796000019	52.4248808897808
0.087812953450079	55.0874612212659
0.098550426314892	57.6779504306929
0.112206724061769	60.6265864834011
0.127759476997186	63.3415731364729
0.145465039759366	66.2037864789212
0.168035843630453	69.131911259623
0.19411176280305	71.9484525505802
0.222083419318477	74.7285290349147
0.259044020108005	77.2129935126797
0.30803890584547	79.7150699642405
0.366294873918129	82.3305792671413
0.435590409221425	84.5720349114709
0.518029785192508	86.3256115446736
0.616085725364177	87.9108051563369
0.732705596850257	89.4631856663669
0.871382022892136	91.1718601604924
1.03629488039837	92.9535006306183
1.23245384670266	94.5235829454768

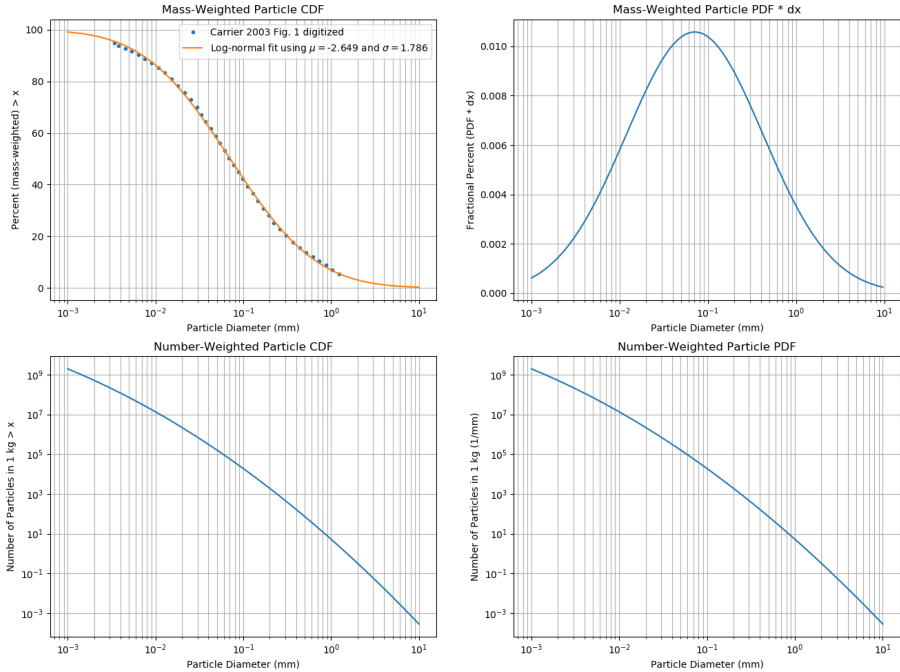


Figure 5: Plots of the mass-weighted and number-weighted CDFs and PDFs derived from [Carrier III \[2003\]](#). Top left: the digitized data from Figure 1 of [Carrier III \[2003\]](#) is shown with the log-normal distribution fit. Top right: The mass-weighted PDF * dx is shown to dictate what particle size dominates the contribution of mass. Bottom left: The number-weighted CDF showing number of particles in 1 kg of regolith greater than a size x . Bottom right: The number-weighted PDF is shown in units of mm^{-1} .

The PDF is then given by

$$f_{\text{kg}}(x) = \frac{1}{\sigma\sqrt{2\pi}} \frac{1}{x} \exp\left[-\frac{(\ln x - \mu)^2}{2\sigma^2}\right]. \quad (2.13)$$

In order to have the number-weighted PDF and CDF, we begin with $f_{\text{kg}}(x)$ and divide by the mass of a given particle size (diameter), [e.g., Equation (7) of [Koschny and Grün, 2001](#)]

$$m(x) = \frac{\pi}{6} \rho x^3, \quad (2.14)$$

so that we have (assuming F_{kg} represents the CDF for 1 kg of regolith)

$$f_{\text{number}}(x) = \frac{f_{\text{kg}}(x)}{m(x)} = \frac{6}{\pi\rho} \frac{1\text{kg}}{1\text{mm}^3} \frac{1}{\sigma\sqrt{2\pi}} \frac{1}{x^4} \exp\left[-\frac{(\ln x - \mu)^2}{2\sigma^2}\right], \quad (2.15)$$

for the number-weighted PDF. To arrive at the number-weighted CFD, integration over $f_{\text{number}}(x)$ is done such that

$$F_{\text{number}}(> x) = \int_x^{\infty} dx' f_{\text{number}}(x'). \quad (2.16)$$

Solving the integral, the number-weighted CDF is given by

$$F_{\text{number}}(> x) = \frac{6}{\pi\rho} \frac{1\text{kg}}{1\text{mm}^3} \frac{1}{\sigma\sqrt{2\pi}} \left[1 - \text{erf}\left(\frac{\ln x - \mu + 3\sigma^2}{\sqrt{2}\sigma}\right) \right] \exp\left(-3\mu + \frac{9\sigma^2}{2}\right), \quad (2.17)$$

which is the number of particles of diameter x or greater in 1 kg of regolith. For $F_{\text{number}}(< x)$, flip the minus sign to a plus sign on the error function. Note that $\text{erfc}(x) = 1 - \text{erf}(x)$.

Fitting the mass-weighted CDF $F(< x)$ to Figure 4, the following parameters are obtained:

$$\mu = -2.649, \quad (2.18)$$

$$\sigma = 1.786, \quad (2.19)$$

where the mean, median, and mode particle size (weighted by mass) is

$$x_{\text{mean}} = \exp\left(\mu + \frac{\sigma^2}{2}\right) = 34.8\mu\text{m}, \quad (2.20)$$

$$x_{\text{median}} = \exp(\mu) = 7.07\mu\text{m}, \quad (2.21)$$

$$x_{\text{mode}} = \exp(\mu - \sigma^2) = 0.291\mu\text{m}. \quad (2.22)$$

If the mean, median, and mode particle size weighted by number are needed, then the modified parameters are

$$\mu^* = \mu - 3\sigma^2 = -12.22, \quad (2.23)$$

$$\sigma^* = \sigma = 1.786, \quad (2.24)$$

giving the following (now weighted by number):

$$x_{\text{mean}}^* = \exp\left(\mu^* + \frac{\sigma^{*2}}{2}\right) = 2.43\text{ nm}, \quad (2.25)$$

$$x_{\text{median}}^* = \exp(\mu^*) = 0.494\text{ nm}, \quad (2.26)$$

$$x_{\text{mode}}^* = \exp(\mu^* - \sigma^{*2}) = 0.0203\text{ nm}. \quad (2.27)$$

Note that these set of averages are outside the range of the data provided in [Carrier III \[2003\]](#) and are only valid if the log-normal distribution holds for these very small particles. This regime is on the order of several atomic nuclei large.

As an example, if the number of particles greater than 1 μg per 1 kg of regolith are needed, then use Equation (2.17) (assuming a regolith density of $\rho = 3.1\text{ g/cm}^3$ such that $x(1\mu\text{g}) = 8.509\mu\text{m}$)

$$F_{\text{number}}(> x = 8.509\mu\text{m}) = 3.146 \times 10^7 \# \text{ of particles per 1 kg of regolith.} \quad (2.28)$$

2.5 Scaling Law Parameters

In the meteoroid ejecta model described in this document, the scaling laws from [Housen and Holsapple \[2011\]](#) are employed. In this section, the parameters of various material types used in fits to the scaling laws are summarized. The specific scaling law equations are discussed in Section 5.

The various sets of parameters for different target materials are given in Table 3 of [Housen and Holsapple \[2011\]](#) with most of them copied here in Table 4, with undefined values filled in that are best represented by either solid, semi-solid, or fine material where applicable. If a material has zero strength, the crater scaling is automatically in the gravity regime and there is no strength regime (and no need for H_2 to be defined).

Table 4: Summary of constants used in the [Housen and Holsapple \[2011\]](#) ejecta model.

Curve no.	C1	C2	C3	C4	C5	C6	C7	C8
Target	Water	Rock	WCB	Sand	Sand	GMS	SFA	PS
Porosity	~ 0	~ 0	20%	35 ± 5%	35 ± 5%	36%	45%	60%
μ	0.55	0.55	0.46	0.41	0.41	0.45	0.4	0.35
C_1	1.5	1.5	0.18	0.55	0.55	1.0	0.55	0.6
k	0.2	0.3	0.3	0.3	0.3	0.5	0.3	0.32
H_1	0.68	0.68* ¹	0.5* ²	0.59	0.59	0.8	0.59* ³	0.59* ³
H_2	—	1.2	0.38	—	—	—	0.4	0.81
$n_{2,G}$	1.5	1.5	1.3* ³	1.3	1.3	1.3	1.2* ²	1.2* ²
p	0.5	0.5	0.3	0.3	0.3	0.3	0.3	0.2
Y (MPa)	0	30	0.45	0	0	0	4×10^{-3}	2×10^{-3}

Note: WCB = weakly cemented basalt, GMS = glass micro-spheres, PS = perlite/sand mixture, SFA = sand/fly ash. All cases shown in this table used: $\nu = 0.4$, $n_1 = 1.2$, $n_{2,S} = 1$, $g = 9.81 \text{ m/s}^2$.

*1 from water, *2 no value given, *3 from sand.

The average regolith porosity from 0 – 60 cm is $46 \pm 2\%$ (see Table 1), so the set of parameters that define SFA (sand/fly ash) are adopted. For a higher fidelity strength, Equation (2.11) can be used instead of $Y = 4 \text{ kPa}$.

3 Primary Flux Environment

3.1 Space-Time Dependence of Environment

The primary environment that is responsible for creating ejecta by impacting the lunar surface varies in both location on the Moon as well as in time. For a time-averaged background environment, the sporadic meteoroid complex (Section 3.2) and near-Earth object (Section 3.3) populations are used as input to the ejecta model over a 19-year time span. Short-term environments may also be generated that have the option to include the meteor showers (Section 3.4, forward work). Time-varying environments can also be generated by providing consecutive ephemeris definitions in

time. If a single time frame is used, it is thought of as the average environment over that time frame.

The location and time span of the primary environment is defined by an ephemeris, or trajectory file, discussed in Section 3.1.1.

3.1.1 Ephemeris Definition

The ephemeris definitions of locations on the Moon are generated by using the service provided by JPL Horizons at ssd.jpl.nasa.gov/horizons/. One way to query their system is to send an email that defines the particular inputs desired, e.g., see Listing 1, which makes it easier to streamline generating many ephemeris files quickly.

Listing 1: An example email that is sent to JPL Horizons to compute an ephemeris file that is centered on the Moon at a location of 90° longitude, –65° latitude, and 0.6 km above the surface for 11 years.

```

1 To: Horizons Ephemeris System <horizons@ssd.jpl.nasa.gov>
2 Subject: JOB
3
4
5 !$$SOF
6 COMMAND= '301'
7 CENTER= 'coord@301'
8 COORD_TYPE= 'GEODETIC'
9 SITE_COORD= '90.0,-65.0,0.6'
10 MAKE_EPHEM= 'YES'
11 TABLE_TYPE= 'VECTORS'
12 START_TIME= '2020-01-01'
13 STOP_TIME= '2039-01-01'
14 STEP_SIZE= '10000'
15 OUT_UNITS= 'KM-S'
16 REF_PLANE= 'ECLIPTIC'
17 REF_SYSTEM= 'J2000'
18 VECT_CORR= 'NONE'
19 VEC_LABELS= 'NO'
20 VEC_DELTA_T= 'NO'
21 CSV_FORMAT= 'NO'
22 OBJ_DATA= 'YES'
23 VEC_TABLE= '3'
24 !$$EOF

```

In order to convert the ephemeris file received from JPL Horizons to a file type that the Meteoroid Engineering Model (MEM) program can read, a Python script is used as shown in Listing 2.

Listing 2: Python script to convert JPL Horizons ephemeris file type to be read into the Meteoroid Engineering Model.

```

1 # Title : ephemeris_parser.py
2 # Project: Lunar Meteoroid Ejecta DSNE Environment
3 # Description: Convert JPL Horizons ephemeris data to MEM readable input

```

```

4  # Author: Anthony M. DeStefano
5  # Company: NASA/MSFC/EV44
6  # E-mail: anthony.m.destefano@nasa.gov
7  # Office phone: 256-544-3094
8  # Date last edited: 3/10/2020
9
10 import glob
11
12 offset = 58 # size of header
13 cycle = 4   # number of rows for a set of data (same JD timestamp)
14
15 for filepath in glob.iglob('Horizons*.txt'):
16     print(filepath)
17     with open(filepath) as fp:
18         with open('MEM_input_' + filepath, 'w') as out_file:
19             out_file.write('#\n#\n#\n#\n#-----JD-----X-----\n'
20                           'Y-----Z-----VX-----VY-----VZ\n')
21             for cnt, line in enumerate(fp):
22                 # skip footer info
23                 if line == '$$EOE\n':
24                     break
25                 # skip header info
26                 if cnt > offset-1:
27                     # Read Julian Date
28                     if (cnt - offset) % cycle == 0:
29                         out_file.write(line[:17])
30                         # Read position and velocity vector (two sets of 3
31                         components)
32                         elif (cnt - offset) % cycle != 3:
33                             for val in line.split():
34                                 # need -1 to flip vector from origin on the lunar
35                                 # surface to origin to Moon's center
36                                 out_file.write('_' + str(-1.0*float(val)))
37                         # Skip the last vector and print a new line
38                         else:
39                             out_file.write('\n')

```

Several ephemeris files can be used to define local primary environments on the Moon by specifying different latitude-longitude coordinates. As an example, 5-degree increments can be used in latitude going from the north pole⁴ (+90°) to the south pole (-90°) and 90-degrees increments can be used in longitude to define the meridian (0°), eastern limb (+90°), far side (+180°), and the western limb (+270°) locations.

3.2 Sporadic Meteoroid Complex

The primary flux of sporadic meteoroids onto the surface of the Moon changes depending on the selenographic location on the Moon. Because of this effect, ephemeris data⁵ was generated for different latitudes and longitudes on the Moon in 5-degree increments from pole to pole, and in 90-degree increments in longitude. A time frame of 19 years was chosen, or a Metonic cycle, which takes into account many different Sun-Earth-Moon geometries. The Meteoroid Engineering Model (MEM) [Moorhead

⁴The poles must not be exactly ±90°, but offset slightly to avoid errors in the JPL Horizons system.

⁵Horizons Ephemeris System <horizons@ssd.jpl.nasa.gov>.

et al., 2019] is used to generate the sporadic meteoroids, i.e., the background flux.

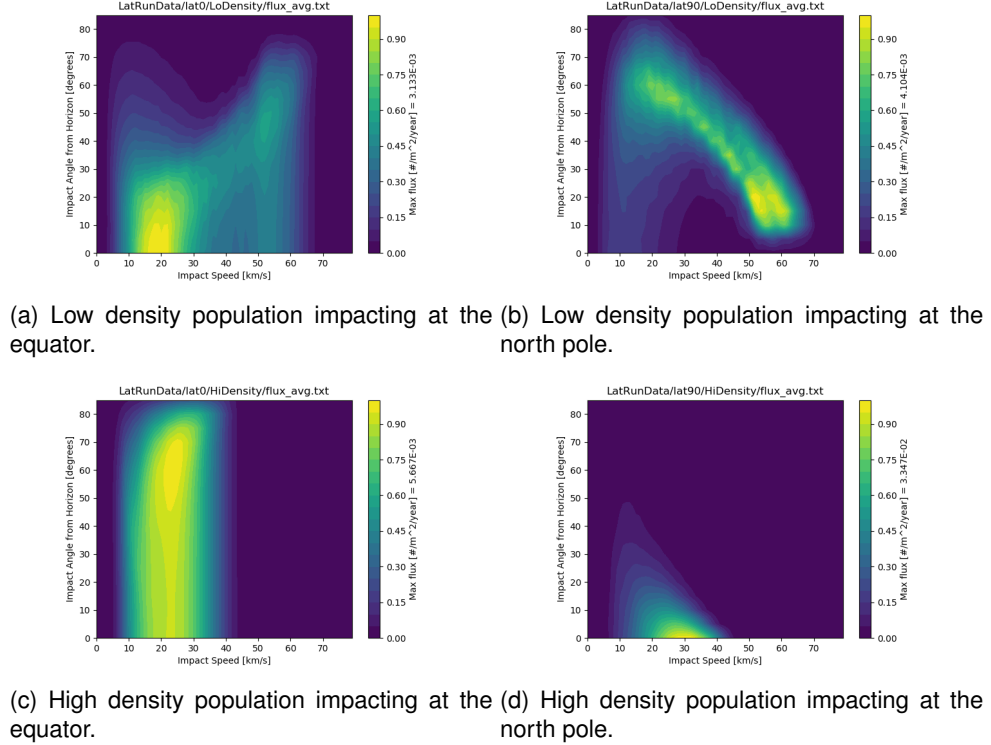


Figure 6: Fluxes at the meridional plane (as a function of impact speed and angle from the horizon) of the low density population (a) and (b), and the high density population (c) and (d) impacting the Moon at the equator (a) and (c), and the north/south pole (b) and (d).

As an example, in Figure 6, the speed-angle flux distribution is shown at the equator and at the poles for the low and high density MEM populations. Note that the fluxes in the northern and southern hemispheres are symmetric about the equator. It can be seen from Figure 6 that the impact angles and speeds are highly dependent on the impact latitude on the Moon and hence warrant a more sophisticated approach to computing the secondary fluxes. It cannot be assumed that most impacts are at 45 degrees or are not highly oblique.

Other time frames may be simulated, such a week, a month, or a year, and can also vary as a function of time. In the current model output, a 19-year averaged flux is used.

3.2.1 Angular Distribution

The angular distribution of the primary fluxes can be viewed in a Mollweide and all-sky (polar) projection for both the low- and high-density components of the sporadic meteoroids. Three specific latitudinal regions are depicted in Figures 7, 8, and 9 for the south pole, -45° latitude, and the equator, respectively, at the central meridian (0° longitude).

The fluxes from the low- and high-density components seem to originate from opposing locations in the sky [e.g., see Figure 2.2 of [Moorhead et al., 2019](#)]. The shift is due to the high-density population meteoroids coming from mainly the ecliptic plane (helion and anti-helion sources) while the low-density population tends to come from higher inclinations (toroidal and apex sources).

The figures that follow show a departure from a purely isotropic flux source and the effect on the impact angle on the planetary surface. As shown in [Pierazzo and Melosh \[2000\]](#), the probability of hitting a planetary body, regardless of the target's gravitational field, is given by

$$dP = 2 \sin \alpha \cos \alpha d\alpha, \quad (3.1)$$

where α is the angle from zenith. This equation shows that the most probable impact angle is at 45° , which is not supported by the sporadic meteoroid fluxes, implying a non-isotropic origin – known to be the helion/anti-helion, toroidal, and apex sources.

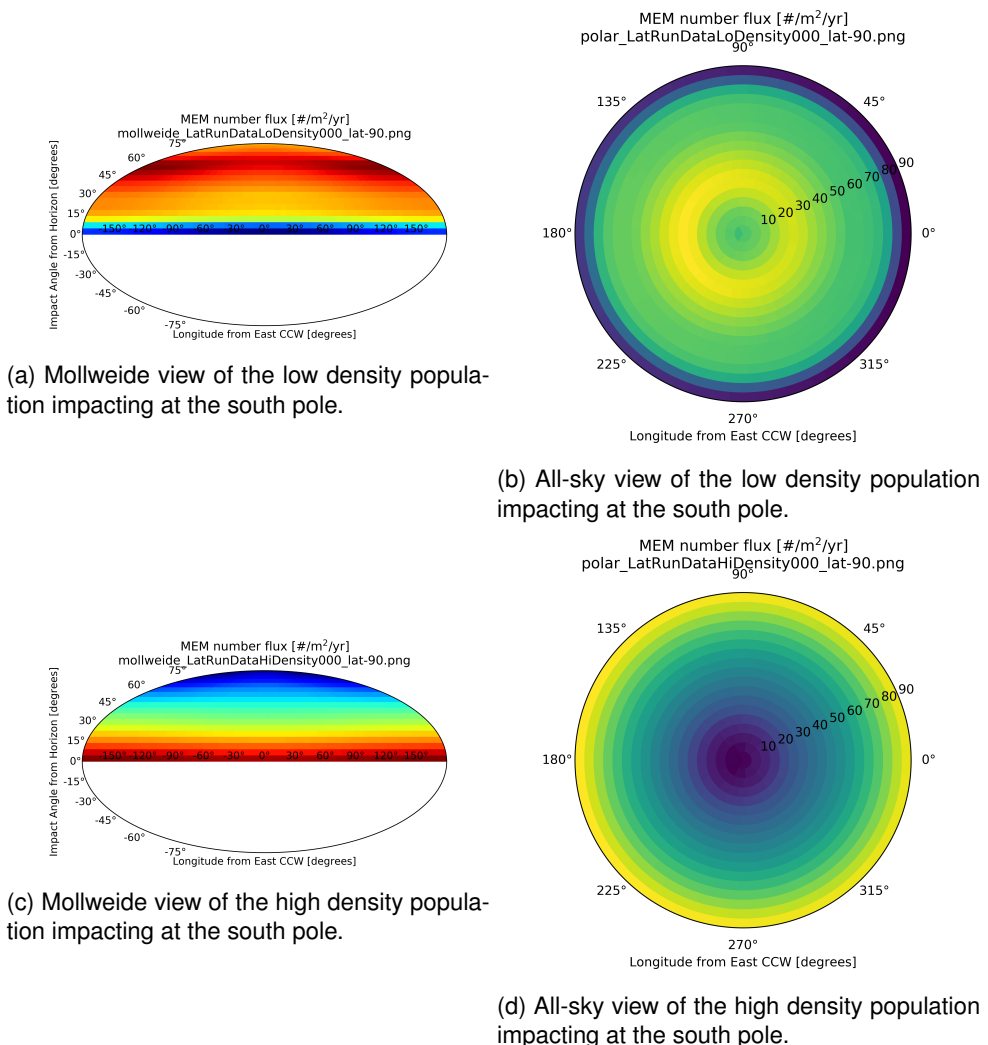


Figure 7: Fluxes at the meridional plane as a function of approaching angle for the low density population (a) and (b), and the high density population (c) and (d) impacting the Moon at the south pole in a Mollweide (a) and (c), and all-sky (b) and (d) projection.

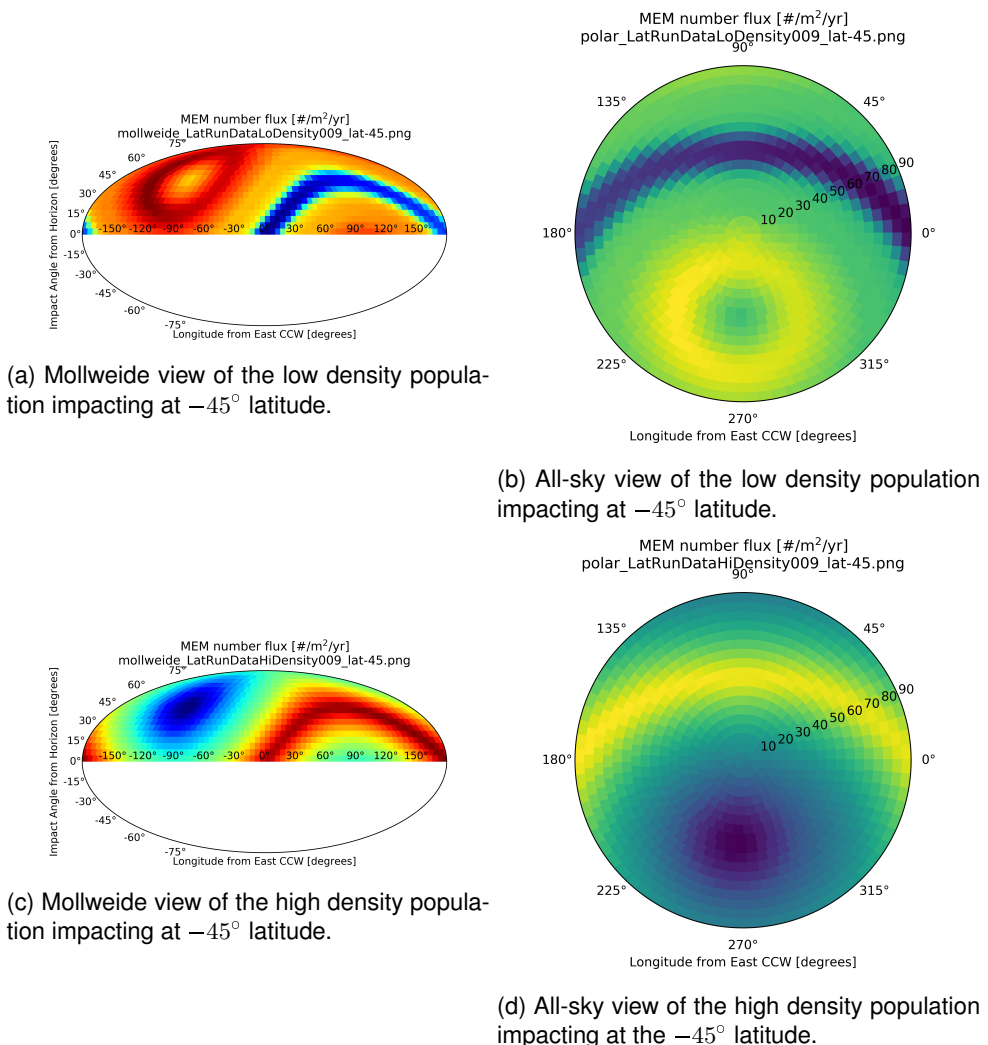


Figure 8: Fluxes at the meridional plane as a function of approaching angle for the low density population (a) and (b), and the high density population (c) and (d) impacting the Moon at -45° latitude in a Mollweide (a) and (c), and all-sky (b) and (d) projection.

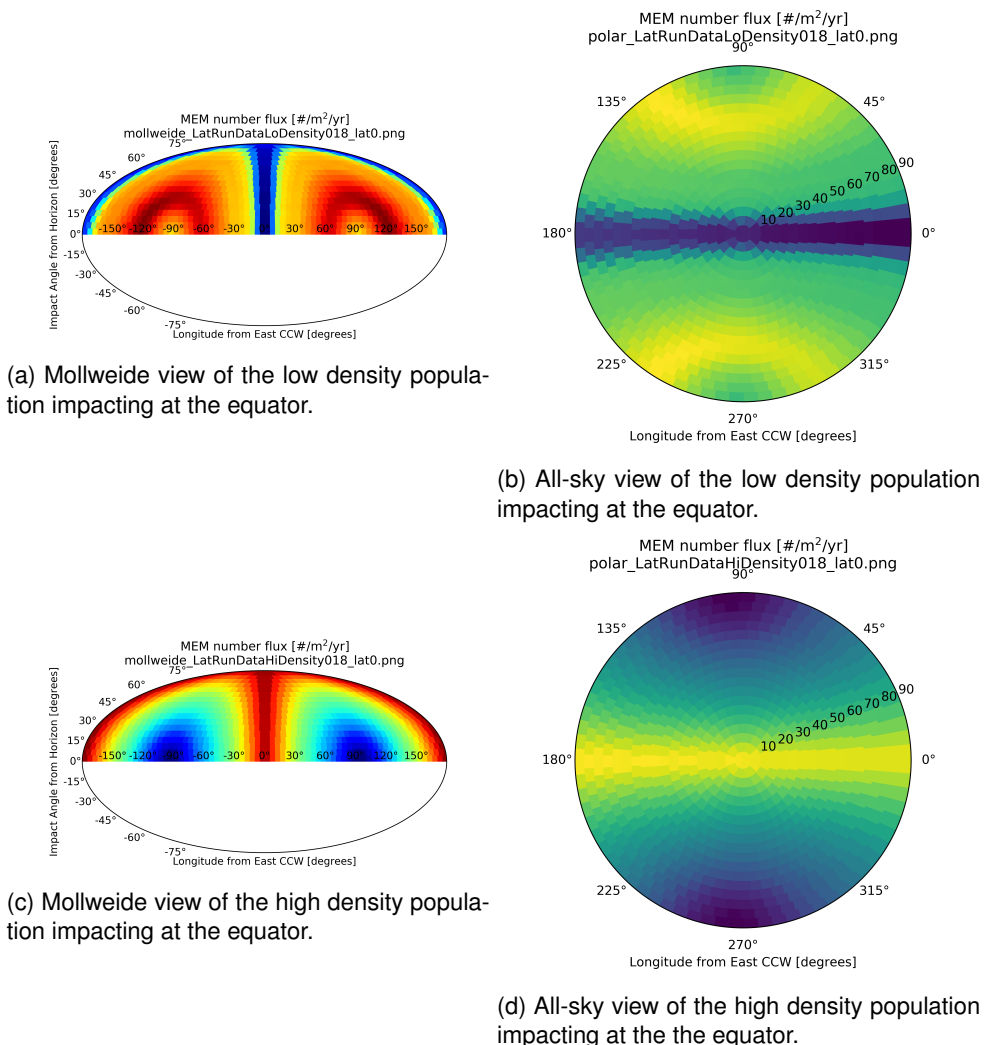


Figure 9: Fluxes at the meridional plane as a function of approaching angle for the low density population (a) and (b), and the high density population (c) and (d) impacting the Moon at the equator in a Mollweide (a) and (c), and all-sky (b) and (d) projection.

3.2.2 Density Distribution

The meteoroid density has two components, a low and a high density contribution, as shown in Figure 10. The meteoroid density components can be written in terms of log-normal distributions

$$F_\delta(x) = \frac{A}{\sigma\sqrt{2\pi}x} \exp\left[-\frac{(\ln x - \mu_\delta)^2}{2\sigma^2}\right], \quad (3.2)$$

where the fit parameters for the low and high density components are shown in Figures 11 and 12.

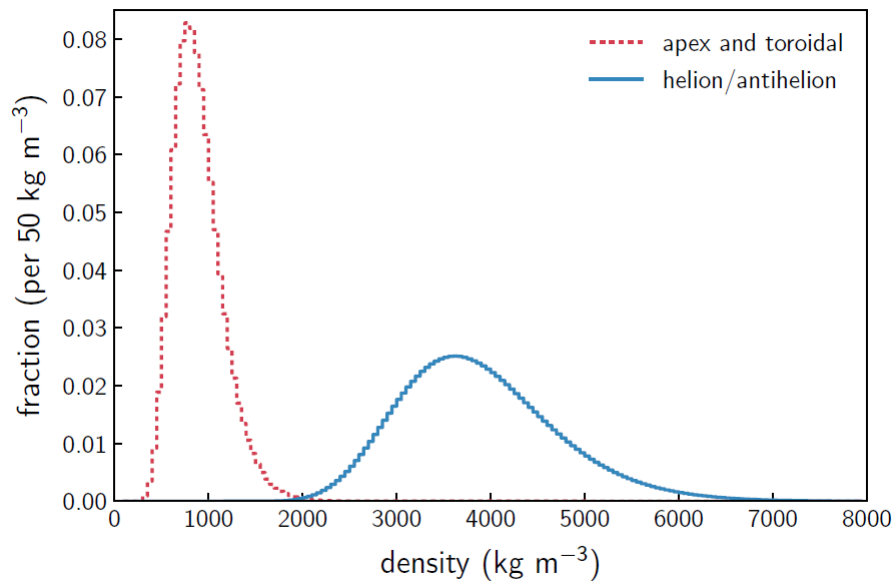


Figure 10: Meteoroid density distribution according to the MEM3 User Guide. The apex and toroidal meteoroid sources constitute the low-density population, while the helion/antihelion source constitutes the high-density population. Each set of densities follows a log-normal distribution [c.f. Figure 11, [Moorhead et al., 2019](#)].

```
[1/2/2020 5:16:00 PM      Plot: "Graph5"]
Non-linear fit of dataset: Table3_2, using function: log10(a/((10^x)*s*2.506628275)*exp(-(x*ln(10)-m)^2/(2*s^2)))
Y standard errors: Unknown
Scaled Levenberg-Marquardt algorithm with tolerance = 0.0001
From x = 2.097 to x = 3.902
a = 53.839135327051 +/- 0.82189223780795
s = 0.294917539134767 +/- 0.000210957288819632
m = 6.7346464600191 +/- 0.00131007263737737
-----
Chi^2 = 0.305039664208057
R^2 = 0.999894109124399
-----
Iterations = 0
Status = success
```

Figure 11: Non-linear fit of the low density profile in Figure 10 with Eq. 3.2 in SciDAVis, giving the constants for $a \rightarrow A$, $s \rightarrow \sigma$, and $m \rightarrow \mu_\delta$.

```
[1/2/2020 5:19:18 PM      Plot: "Graph6"]
Non-linear fit of dataset: Table4_2, using function: log10(a/((10^x)*s*2.506628275)*exp(-(x*ln(10)-m)^2/(2*s^2)))
Y standard errors: Unknown
Scaled Levenberg-Marquardt algorithm with tolerance = 0.0001
From x = 2.096910013 to x = 3.901730692
a = 39.742506482046 +/- 1.58430260083343
s = 0.221066131940955 +/- 0.00039359322394943
m = 8.26026111215463 +/- 0.00352064330966803
-----
Chi^2 = 5.98458401110512
R^2 = 0.999293469696896
-----
Iterations = 0
Status = iteration is not making progress towards solution
```

Figure 12: Non-linear fit of the high density profile in Figure 10 with Eq. 3.2 in SciDAVis, giving the constants for $a \rightarrow A$, $s \rightarrow \sigma$, and $m \rightarrow \mu_\delta$.

3.2.3 Mass Distribution

From the MEM3 User Guide , we get the $g(m)$ flux of meteoroids larger than a limiting mass m , originally from [Grün et al. \[1985\]](#). The Grün interplanetary flux equation is given by

$$g(m) = (c_4 m^{\gamma_4} + c_5)^{\gamma_5} + c_6 (m + c_7 m^{\gamma_6} + c_8 m^{\gamma_7})^{\gamma_8} + c_9 (m + c_{10} m^{\gamma_9})^{\gamma_{10}}, \quad (3.3)$$

where the constants are $c_4 = 2.2 \times 10^3$, $c_5 = 15$, $c_6 = 1.3 \times 10^{-9}$, $c_7 = 10^{11}$, $c_8 = 10^{27}$, $c_9 = 1.3 \times 10^{-16}$, $c_{10} = 10^6$; and the exponents are $\gamma_4 = 0.306$, $\gamma_5 = -4.38$, $\gamma_6 = 2$, $\gamma_7 = 4$, $\gamma_8 = -0.36$, $\gamma_9 = 2$, and $\gamma_{10} = -0.85$. Equation 3.3 is applied to MEM's mass range and is shown in Figure 13.

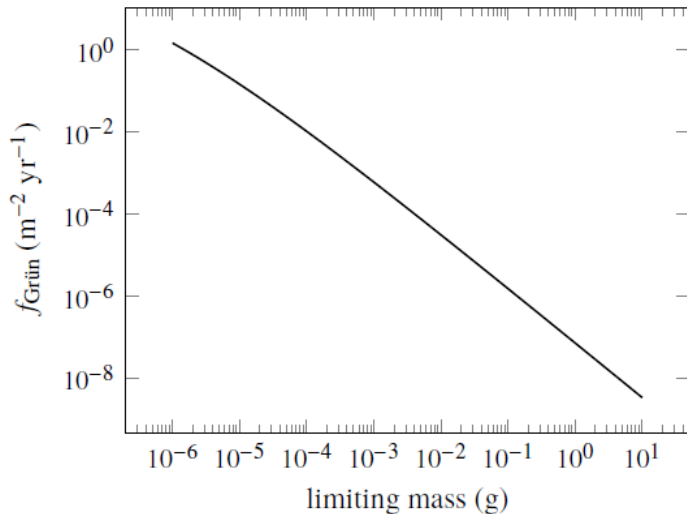


Figure 13: The Grün interplanetary meteoroid flux as a function of limiting particle mass [[Moorhead et al., 2019](#), Figure 1], normalized to 1 for a limiting mass equal to or greater than $1\mu\text{g}$.

3.3 Near-Earth Objects

The near-Earth objects (NEOs) described in this model consist of the small asteroids and comets between about 0.1 m and 1000 m diameter onto the lunar surface [[Moorhead, 2020](#)]. The speed and mass distributions (Sections 3.3.1 and 3.3.2) were based on [Brown et al. \[2002\]](#) and the Center for Near Earth Object Studies (CNEOS)⁶, respectively. Both of the data sources are kinetic-energy-limited and correspond to the impact flux at the Earth's atmosphere, translated to fluxes onto the lunar surface [[Moorhead, 2020](#)].

⁶<https://cneos.jpl.nasa.gov/fireballs/>

3.3.1 Speed Distribution

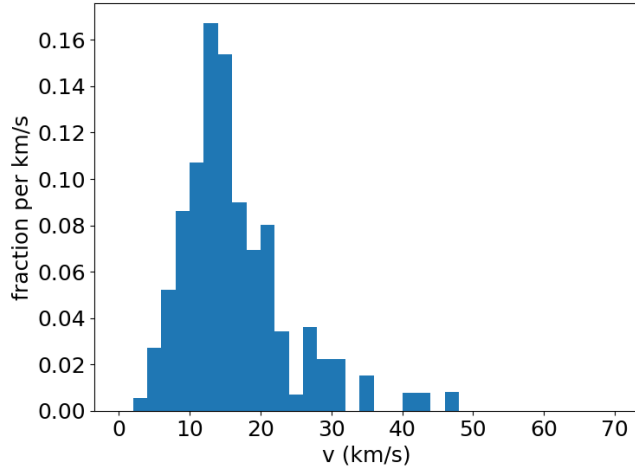


Figure 14: Mass-limited speed distribution at the lunar surface.

The speed distribution of NEO’s is shown in Figure 14. The values (fraction of flux per bin) in each bin are midpoint values, where the bins have a size of 2 km s^{-1} . Note also that because the flux is a power law, this speed distribution is independent of limiting mass.

3.3.2 Mass Distribution

The mass-limited flux at the lunar surface can be shown to be [see, *Moorhead, 2020*]

$$g_{\mathbb{C}}(m) = 2.89 \times 10^{-11} \text{ m}^{-2} \text{ yr}^{-1} \cdot m^{-0.9}, \quad (3.4)$$

where m is the mass of the impactor in kg. Since the mass-limited flux has a power-law index greater than -1 , a maximum impactor size should be defined. An example of quantifying the largest size could be by computing the size that would have an n -% chance of hitting the Moon in Y years. If $n = 5\%$ and $Y = 10$ years, then the largest size would be

$$\begin{aligned} m_{max,kg} &= \left(\frac{2.89 \times 10^{-11} \text{ m}^{-2} \text{ yr}^{-1} \cdot 3.793 \times 10^{13} \text{ m}^{-2} \cdot 10 \text{ yr}}{0.05} \right)^{1/0.9} \\ &= 2.4 \times 10^5 \text{ kg}. \end{aligned} \quad (3.5)$$

If the NEO density is assumed to be 3.0 g/cm^3 (which is the assumption used throughout the model), then this corresponds to a diameter of 5.3 m .

3.4 Meteoroid Showers

The primary fluxes that originate from meteoroid showers can also produce ejecta. However, each different meteoroid shower has its own strength, duration, and time of year at which they occur. A prediction of the meteoroid shower fluxes as a function of time are compared to the sporadic meteoroids at different limiting energies, shown in Figure 15 [Moorhead et al., 2020].

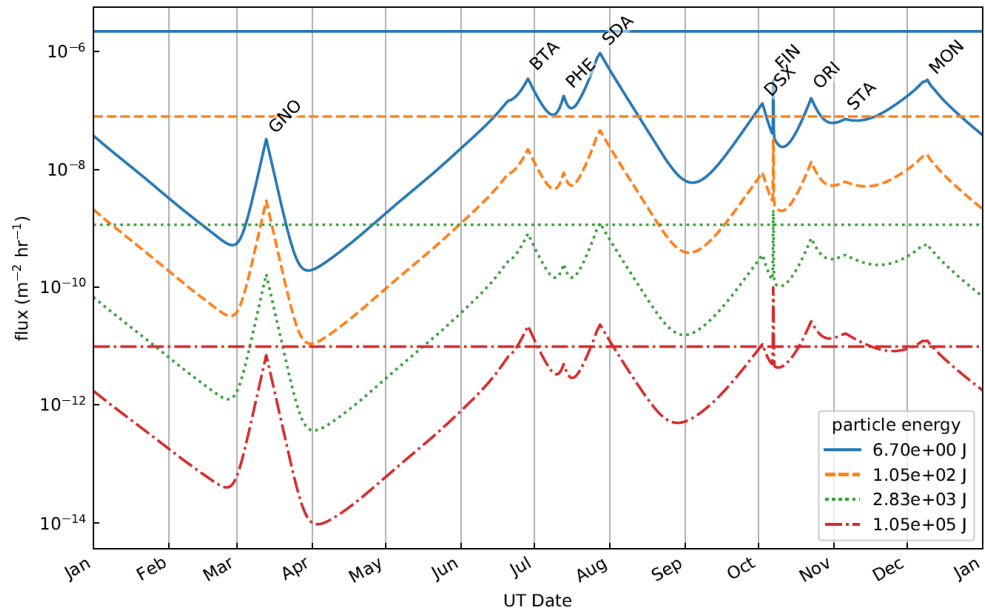


Figure 15: Meteor shower flux (variable lines) and sporadic meteoroid flux (horizontal lines) over the course of 2021. Fluxes are quoted to four limiting particle kinetic energies; these kinetic energies correspond to particles with diameters of 0.04 cm, 0.1 cm, 0.3 cm, and 1 cm, assuming a density of 1 g cm^{-3} and a speed of 20 km s^{-1} , [see Figure 1, Moorhead et al., 2020].

At this time, it is assumed that the ejecta produced by meteoroid showers is small compared to the ejecta produced by the sporadic meteoroids. Further investigation may be warranted, however, short-term ejecta environments may need to include meteoroid showers during a particularly strong shower. These operational environments would be created on an as-need basis for lunar surface EVAs, similar to forecasts for meteoroid showers for ISS EVAs.

4 Ejecta Flux from Impact Point

The ejected mass from an impact is distributed at different speeds (Section 4.1.1), angles (Sections 4.1.2 and 4.1.3), and sizes (Section 4.2). The speed and size of the ejecta is assumed to be dependent on each other – the larger the ejected particle the slower, on average, the particle that is ejected. The impactor impact angle and azimuth determines the zenith and azimuth distribution of the ejecta. For more oblique impacts, the ejecta is projected less from normal and more towards the horizon, in addition to having a stronger component downstream with respect to the impactor azimuth in terms of the ejecta azimuth distribution.

4.1 Ejecta Distribution

4.1.1 Speed Distribution

The speed distribution of the ejecta is determined by the scaling laws [[Housen and Holsapple, 2011](#)] that are assumed in this model (see Section 5). As an approximation, the speed distribution can be described by a power-law distribution with an index that depends on the target material. However, a more complete speed distribution is used that not only includes a power-law regime, but includes proper cut-offs for the slowest speeds and fastest speeds, discussed in Section 5.2.

4.1.2 Zenith Distribution

The ejecta zenith distribution is typically peaked at some zenith angle α_{max} that falls off at other angles. The peak zenith angle α_{max} can have different dependencies on the impactor properties.

Constant Zenith Peak: The simplest case is a constant, $\alpha_{max} = \alpha_0$, typically taken as $\alpha_0 = \pi/4$. For relatively close impact distances, an ejected angle of 45° gives the most efficient ejecta – the ejecta travels further for a given speed.

Impact Angle Dependent Zenith Peak: To include more information into the ejecta blanket from the impactor is to have the zenith peak as a function of the impact angle, $\alpha_{max} = \alpha_{max}(\alpha_i)$, where α_i is the impact angle of the impactor. For simplicity, the peak zenith angle can be taken as the downstream for all azimuth, given in Equation (4.1).

Impact Angle & Azimuth Dependent Zenith Peak: An increased fidelity peak zenith angle also include information about the impactor azimuth angle, $\alpha_{max} = \alpha_{max}(\alpha_i, \beta_i)$, where β_i is the impact azimuth.

The peak zenith angle can be modeled after experiments of oblique impacts following Figure 18 of [[Gault and Wedekind \[1978\]](#)] as a proxy to the model of α_{max} . Using

a third-order polynomial for both fits to the downstream and upstream angles given in Table 5, the peak zenith angles downstream and upstream are given by

$$\alpha_{max}(\beta - \beta_i = 0) = 0.0003\alpha_i^3 - 0.036\alpha_i^2 + 1.5206\alpha_i + 20, \text{ downstream} \quad (4.1)$$

$$\alpha_{max}(\beta - \beta_i = \pi) = -0.00042\alpha_i^3 + 0.0236\alpha_i^2 + 0.129\alpha_i + 20, \text{ upstream} \quad (4.2)$$

in units of degrees, where β is the ejecta azimuth. When both the impact and ejecta azimuth angles are in the same direction (i.e., $\beta - \beta_i = 0$), this is downstream.

Table 5: Cone angles of upstream and downstream of impact derived from Figure 18 of *Gault and Wedekind [1978]*.

Impact Zenith Angle	Upstream Zenith Angle	Downstream Zenith Angle
0	20	20
15	24	35
30	35	45
45	28	40
60	13	54
75	-35	66

Rival & Mandeville (Gaussian Distribution): One example of a peaked distribution is given in *Rival and Mandeville [1999]*, shown below for reference:

$$F(\alpha) = \frac{1}{\sigma\sqrt{2\pi}} \exp\left[-\frac{(\alpha - \alpha_{max})^2}{2\sigma^2}\right], \quad (4.3)$$

where α_{max} is defined as

$$\alpha_{max} = \begin{cases} \frac{\alpha_{max60} - \alpha_{max0}}{\pi/3} \alpha_i + \alpha_{max0} & \text{for } \alpha_i \leq \pi/3 = 60^\circ \\ \alpha_{max60} & \text{for } \alpha_i > \pi/3 = 60^\circ \end{cases}, \quad (4.4)$$

for α_i the impact zenith angle, and [see *Miller, 2017*]

$$\alpha_{max0} = \frac{\pi}{6} = 30^\circ, \quad (4.5)$$

$$\alpha_{max60} = \frac{4\pi}{9} = 80^\circ, \quad (4.6)$$

$$\sigma = \frac{\pi}{60} = 3^\circ, \quad (4.7)$$

where the peak ejecta angle is shifted from 30° of zenith for a normal impact to 80° of zenith for oblique impacts ($> 60^\circ$).

One difficulty with this zenith distribution is the normalization, assuming ejecta is only created from $0 < \alpha < \pi/2$. A Gaussian distribution is usually integrated from $-\infty$ to $+\infty$, so a finite integration introduces error functions.

Raised Cosine Distribution: A more focused zenith distribution that is easier to normalize can be described by a raised cosine distribution, given as

$$F(\alpha) = \begin{cases} \frac{1}{2s} \left[1 + \cos \left(\frac{\alpha - \mu}{s} \pi \right) \right], & \text{for } \mu - s \leq \alpha \leq \mu + s \\ 0, & \text{otherwise} \end{cases}, \quad (4.8)$$

This distribution is symmetric about the peak μ , with a spread s . It is assumed that $\mu - s \geq 0$ and $\mu + s \leq \pi/2$, otherwise the normalization term would be dependent on the peak, in addition to the spread.

4.1.3 Azimuth Distribution

The azimuth distribution is often dependent on the impactor azimuth such that there are more ejecta downstream for oblique impacts. Normal impacts are expected to produce a symmetric azimuth distribution. For highly oblique impacts ($\alpha_i > \pi/3$) there is often seen a *butterfly pattern* [Shuvalov, 2011]. However, over a large number of oblique impacts of various sizes, it is plausible to assume that the direct downstream direction dominates the azimuth distribution.

Rival & Mandeville: An example azimuth distribution can be found in [Rival and Mandeville \[1999\]](#), given by

$$G(\beta) = \begin{cases} \frac{1}{2\pi} \left[1 + \frac{3\alpha_i}{2\pi - 3\alpha_i} \cos(\beta - \beta_i) \right] & \text{for } \alpha_i \leq \pi/3 = 60^\circ \\ \frac{1}{\sigma' \sqrt{2\pi}} \exp \left[-\frac{(\beta - \beta_i)^2}{2\sigma'^2} \right] & \text{for } \alpha_i > \pi/3 = 60^\circ \end{cases}, \quad (4.9)$$

where

$$\sigma' = \frac{\pi}{36} = 5^\circ, \quad (4.10)$$

for β_i the impact azimuth angle + π .

Variation on Rival & Mandeville: In order to have a periodic and easy-to-normalize function, the oblique regime is modified from Equation (4.9) to give

$$G(\beta) = \begin{cases} \frac{1}{2\pi} \left[1 + \frac{3\alpha_i}{2\pi - 3\alpha_i} \cos(\beta - \beta_i) \right] & \text{for } \alpha_i \leq \pi/3 = 60^\circ \\ \frac{1 + \cos(\beta - \beta_i)}{2\pi} & \text{for } \alpha_i > \pi/3 = 60^\circ \end{cases}. \quad (4.11)$$

An alteration of Equation (4.11) on the oblique case could be to use a raised cosine distribution with a spread of $s = 3\sigma'$.

4.2 Mass/Particle Size Distribution

The mass or particle size distribution of ejecta can be approximated in a few different ways. For the purpose of comparing to various sources, there are four possible ways

to describe the particle size distribution, give by [Koschny and Grün, 2001]

$$m_{cum}(\leq d) = k_1 d^\alpha, \quad (4.12)$$

$$N_{cum}(\geq m) = k_2 m^{-\beta}, \quad (4.13)$$

$$N_{cum}(\geq d) = k_3 d^\gamma, \quad (4.14)$$

$$m_{cum}(\leq m) = k_4 m^\delta, \quad (4.15)$$

with N_{cum} the cumulative number, m_{cum} the cumulative mass, d the particle diameter, and m the particle mass.

The various transformations between the four possible descriptions are:

$$\beta = -\gamma/3, \quad (4.16)$$

$$\alpha = 3(1 - \beta), \quad (4.17)$$

$$\alpha = \gamma + 3, \quad (4.18)$$

$$\delta = \alpha/3. \quad (4.19)$$

Table IV of [Koschny and Grün, 2001] gives examples of the exponent α , summarized here in Table 6.

Table 6: A compilation of indices of the various particle size distribution descriptions. Values that are in bold are the index that was originally used in the corresponding source.

Target Material	Source	α	β	$-\gamma$
Basalt	Koschny and Grün [2001]	0.56, 0.96	0.81, 0.68	2.44, 2.04
Granite	"	0.44	0.85	2.56
Gabbro	"	1.41	0.53	1.59
Alumina	"	1.08	0.64	1.92
Water ice	"	1.3	0.57	1.7
Porous ice-silicate	"	1.8	0.4	1.2
Compact ice-silicate	"	1.4±0.3	0.53±0.1	1.6±0.3
Basalt	Cour-Palais [1969]	-0.6	1.2	3.6
Sandstone	Buhl et al. [2014]	0.26-0.46	0.85-0.91	2.54-2.74
Apollo Samples	Carrier III [2003]	-0.55	1.18	3.55^a
Basalt + others	O'Keefe and Ahrens [1985]	0.42-0.53	0.82-0.86	2.47-2.58

^a valid for diameters from 10^{-6} m to 10^{-1} m.

4.2.1 NASA SP-8013

The Meteoroid Environment Model - 1969 Near Earth to Lunar Surface [Cour-Palais, 1969], or NASA SP-8013, contains both the primary meteoroid environment as well as the lunar ejecta environment. The latter is given in terms of cumulative number flux of secondary ejecta greater than mass m (i.e., in the form of Equation (4.13)), shown in Figure 16 (Figure 10 of Cour-Palais [1969]).

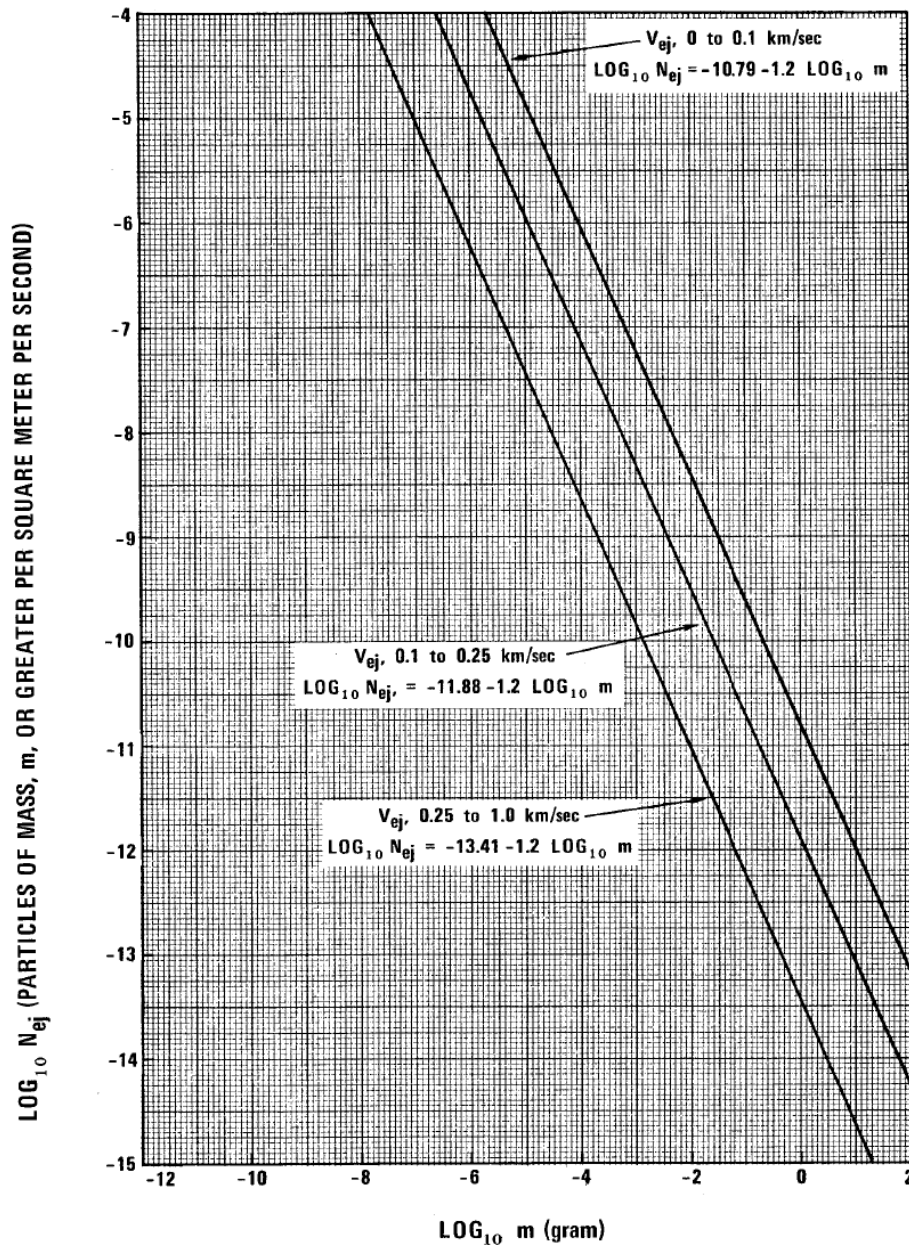


Figure 16: Average cumulative lunar ejecta flux-mass distribution for each of three ejecta velocity intervals [[Cour-Palais, 1969](#)].

Each of the three velocity intervals have a power-law index of $-\beta = -1.2$, corresponding to $\alpha = -0.6$ (see Table 6). Qualitatively, the larger the power-law index α is, the greater number of larger particles are present in the size distribution [e.g., [Koschny and Grün, 2001](#); [Bierhaus et al., 2018](#)]. For a negative α , this implies an absence of larger sized particles in the SP-8013 model compared to what is shown in [Koschny and Grün \[2001\]](#).

The power-law index of $-\beta = -1.2$ is a simplification of [Zook \[1967\]](#), which is what the SP-8013 is based on for lunar ejecta. Figure 5 of [Zook \[1967\]](#) displays three different velocity ranges with $\beta = 1$ for $0 \leq v \leq 100$ m/s, $\beta = 1$ for $100 \leq v \leq 250$ m/s, and $\beta = 1.16$ for $250 \leq v \leq 1000$ m/s.

It is interesting to point out that the particle size distribution shown in Figure 16 has a similar power-law index with the regolith particle size distribution of diameters from 10^{-6} m to 10^{-1} m of [Carrier III \[2003\]](#), see Table 6. Since the regolith particle size distribution is a log-normal distribution, the power-law index for larger diameters will be even more steep, and therefore a more negative α , meaning there is an absence of larger stones or boulders in the top layers of regolith sampled from Apollo.

4.2.2 O'Keefe & Ahrens 1985

A conclusion from [Sachse et al. \[2015\]](#) states that *the assumption that the size of the fragments and the speed at the moment of ejection are uncorrelated* should be dropped. In practice, larger ejected particles typically have slower speeds while smaller ejected particles have faster speeds. This observation is not seen in the previous size distribution model of NASA SP-8013⁷, so another model is sought after.

The particle size distribution discussed in [O'Keefe and Ahrens \[1985\]](#) gives a way to introduce a speed-dependent particle size distribution. The cumulative amount of mass of ejecta fragments of mass greater than m is given by (Equation (11) of [O'Keefe and Ahrens \[1985\]](#)), note $\beta_{OK85} \equiv \alpha$ as in Table 6,

$$f(m, m_{bv}(v)) = 1 - \left(\frac{m}{m_{bv}} \right)^{\frac{\beta_{OK85}}{3}}, \quad (4.20)$$

where the mass of the largest fragment ejected at a given ejected velocity v is

$$\frac{m_{bv}(v)}{m_b} = \left(\frac{v}{v_{min}} \right)^{-\delta_{OK85}}. \quad (4.21)$$

The speed index δ_{OK85} is related to the power-law index of the CDF of mass exceeding a certain speed of ejecta (e.g., 3μ from [Housen and Holsapple \[2011\]](#)) and the CDF of mass not exceeding a certain diameter, i.e. α , given by

$$\delta_{OK85} = \frac{9\mu}{\alpha}. \quad (4.22)$$

⁷It is important to note that [Zook \[1967\]](#) did include a speed dependent size distribution in their model (they looked at three variations, ultimately using a piece-wise power-law model), however, [Cour-Palais \[1969\]](#) in SP-8013 simplified the size distribution to be constant for each of the speed ranges.

The minimum velocity v_{min} is defined as the minimum speed at which an ejected particle can reach the rim of a crater from the bottom of the crater,

$$v_{min} = 2\sqrt{\frac{gR}{K}}, \quad (4.23)$$

where g is the lunar gravitational constant, R is the crater radius (see Section 5.1), and K is the crater diameter-to-depth ratio which typically varies between 5 and 20.

The maximum fragmentation mass is given in *O'Keefe and Ahrens [1985]* as

$$m_b = 0.2M_{tot}^{0.8}, \quad (4.24)$$

where M_{tot} is the total mass ejected from the crater by an impactor. On the other hand, *Koschny and Grün [2001]* have a more conservative estimate on the maximum fragmentation mass with

$$m_b = 0.01M_{tot}. \quad (4.25)$$

4.3 Orbital Mechanics

4.3.1 Crater on Surface to Observer at Surface

4.3.2 Crater on Surface to Observer at or above Surface

4.4 Selenographic Distance & Bearing

Given two latitude-longitude points on a sphere, (ϕ_1, λ_1) and (ϕ_2, λ_2) , the distance and bearing can be computed following Chris Veness's webpage⁸.

The distance D is given by the equation

$$\tan\left(\frac{D}{2r_m}\right) = \sqrt{\frac{a}{1-a}}, \quad (4.26)$$

where a is given by

$$a = \sin^2(\Delta\phi/2) + \cos\phi_1 \cos\phi_2 \sin^2(\Delta\lambda/2), \quad (4.27)$$

for $\Delta\phi = \phi_1 - \phi_2$ and $\Delta\lambda = \lambda_1 - \lambda_2$. Solving for the distance and simplifying,

$$D = 2r_m \arcsin(\sqrt{a}), \quad (4.28)$$

or

$$D = 2r_m \arccos(\sqrt{1-a}). \quad (4.29)$$

Other useful expressions involving trigonometric functions of D/r_m are

$$\sin(D/r_m) = 2\sqrt{a(1-a)}, \quad (4.30)$$

$$\cos(D/r_m) = 1 - 2a, \quad (4.31)$$

$$\tan(D/r_m) = \frac{2\sqrt{a(1-a)}}{1-2a}. \quad (4.32)$$

⁸<https://www.movable-type.co.uk/scripts/latlong.html>

Equation (4.26) is the shortest distance between two coordinate points. For the long-distance, use

$$\tan\left(\pi - \frac{D}{2r_m}\right) = -\tan\left(\frac{D}{2r_m}\right) = -\sqrt{\frac{a}{1-a}}. \quad (4.33)$$

The initial bearing θ (from due north) is given by the following equation (assuming the short-distance):

$$\tan \theta_{i(1,2)} = \frac{\sin \Delta\lambda \cos \phi_2}{\cos \phi_1 \sin \phi_2 - \sin \phi_1 \cos \phi_2 \cos \Delta\lambda}. \quad (4.34)$$

To find the final bearing (assuming the short-distance), swap $\phi_1 \longleftrightarrow \phi_2$ and $\lambda_1 \longleftrightarrow \lambda_2$ and reverse the angle such that

$$\theta_{f(1,2)} = (\theta_{i(2,1)} + \pi) \bmod 2\pi. \quad (4.35)$$

In order to compute the initial and final bearing for the long-distance trajectory, add π and then mod by 2π to Equations (4.34) and (4.35). In other words, swap initial and final bearings $\theta_{i(1,2)} \longleftrightarrow \theta_{f(1,2)}$.

The final latitude and longitude can also be obtained if the distance D and bearing θ from the starting location are given. The latitude and longitude are given by

$$\phi_2 = \arcsin [\sin \phi_1 \cos(D/r_m) + \cos \phi_1 \sin(D/r_m) \cos \theta], \quad (4.36)$$

$$\lambda_2 = \lambda_1 + \arctan \left[\frac{\sin \theta \sin(D/r_m) \cos \phi_1}{\cos(D/r_m) - \sin \phi_1 \sin \phi_2} \right]. \quad (4.37)$$

5 Scaling Laws

5.1 Crater Size – Strength & Gravity Regime

5.2 Minimum & Maximum Ejected Speed

5.3 Maximum Ejected Particle Mass

5.4 Mass Ejected from Crater

6 Secondary Environment at Asset

6.1 Latitude-Longitude Dependence

6.2 Speed Distribution

6.3 Angular Distribution

6.4 Ejecta Size Distribution

References

- Bierhaus, E., A. S. McEwen, S. Robbins, K. Singer, L. Dones, M. Kirchoff, and J.-P. Williams, Secondary craters and ejecta across the solar system: Populations and effects on impact-crater-based chronologies, *Meteoritics & Planetary Science*, 53(4), 638–671, 2018.
- Brown, P., R. Spalding, D. O. ReVelle, E. Tagliaferri, and S. Worden, The flux of small near-earth objects colliding with the earth, *Nature*, 420(6913), 294, 2002.
- Buhl, E., F. Sommer, M. H. Poelchau, G. Dresen, and T. Kenkmann, Ejecta from experimental impact craters: Particle size distribution and fragmentation energy, *Icarus*, 237, 131–142, 2014.
- Carrier, W. D., Lunar soil grain size distribution, *The moon*, 6(3-4), 250–263, 1973.
- Carrier III, W. D., Particle size distribution of lunar soil, *Journal of Geotechnical and Geoenvironmental Engineering*, 129(10), 956–959, 2003.
- Cour-Palais, B. G., Meteoroid environment model 1969 (near earth to lunar surface), nasa sp-8013, *National Aeronautics and Space Administration, Washington, DC*, 1969.
- Gault, D. E., and J. A. Wedekind, Experimental studies of oblique impact, in *Lunar and Planetary Science Conference Proceedings*, vol. 9, pp. 3843–3875, 1978.
- Grün, E., H. Zook, H. Fechtig, and R. Giese, Collisional balance of the meteoritic complex, *Icarus*, 62(2), 244–272, 1985.
- Heiken, G. H., D. T. Vaniman, and B. M. French, *Lunar Sourcebook, a user's guide to the Moon*, Cambridge University Press, 1991.
- Housen, K. R., and K. A. Holsapple, Ejecta from impact craters, *Icarus*, 211(1), 856–875, 2011.
- Koschny, D., and E. Grün, Impacts into ice–silicate mixtures: Ejecta mass and size distributions, *Icarus*, 154(2), 402–411, 2001.
- Miller, A., Esabase2 debris release 10.0 technical description, *Tech. Rep. 1.7*, ESA, 2017.
- Moorhead, A. V., Osma/meo/lunar-001, *Tech. rep.*, NASA, 2020.
- Moorhead, A. V., A. Kingery, and S. Ehlert, Nasa's meteoroid engineering model 3 and its ability to replicate spacecraft impact rates, *Journal of Spacecraft and Rockets*, pp. 1–17, 2019.
- Moorhead, A. V., W. J. Cooke, and D. E. Moser, The 2021 meteor shower activity forecast for the lunar south pole, *Tech. rep.*, NASA, MEO, 2020.

- O'Keefe, J. D., and T. J. Ahrens, Impact and explosion crater ejecta, fragment size, and velocity, *Icarus*, 62(2), 328–338, 1985.
- Pierazzo, E., and H. Melosh, Understanding oblique impacts from experiments, observations, and modeling, *Annual Review of Earth and Planetary Sciences*, 28(1), 141–167, 2000.
- Rival, M., and J. Mandeville, Modeling of ejecta produced upon hypervelocity impacts, *Space debris*, 1(1), 45–57, 1999.
- Sachse, M., J. Schmidt, S. Kempf, and F. Spahn, Correlation between speed and size for ejecta from hypervelocity impacts, *Journal of Geophysical Research: Planets*, 120(11), 1847–1858, 2015.
- Shuvalov, V., Ejecta deposition after oblique impacts: An influence of impact scale, *Meteoritics & Planetary Science*, 46(11), 1713–1718, 2011.
- Singer, K. N., B. L. Jolliff, and W. B. McKinnon, Lunar secondary craters and estimated ejecta block sizes reveal a scale-dependent fragmentation trend, *Journal of Geophysical Research: Planets*, 125(8), e2019JE006313, 2020.
- Slyuta, E., Physical and mechanical properties of the lunar soil (a review), *Solar System Research*, 48(5), 330–353, 2014.
- Zook, H. A., The problem of secondary ejecta near the lunar surface., in *Transactions of the 1967 National Symposium on Saturn V/Apollo and Beyond*, vol. I, pp. EN–8, 1967.